

Passive Flow Control in Twin Air-Intakes

Akshoy R. Paul, Pritanshu Ranjan, Ravi R. Upadhyay, Anuj Jain

Abstract—Aircraft propulsion systems often use Y-shaped subsonic diffusing ducts as twin air-intakes to supply the ambient air into the engine compressor for thrust generation. Due to space constraint, the diffusers need to be curved, which causes severe flow non-uniformity at the engine face. The present study attempt to control flow in a mild-curved Y-duct diffuser using trapezoidal-shaped vortex generators (VG) attached on either both the sidewalls or top and bottom walls of the diffuser at the inflexion plane. A commercial computational fluid dynamics (CFD) code is modified and is used to simulate the effects of SVG in flow of a Y-duct diffuser. A few experiments are conducted for CFD code validation, while the rest are done computationally. The best combination of Y-duct diffuser is found with VG-2 arranged in co-rotating sequence and attached to both the sidewalls, which ensures highest static pressure recovery, lowest total pressure loss, minimum flow distortion and less flow separation in Y-duct diffuser. The decrease in VG height while attached to top and bottom walls further improves axial flow uniformity at the diffuser outlet by a great margin as compared to the bare duct.

Keywords—Twin air-intake, Vortex generator (VG), Turbulence model, Pressure recovery, Distortion coefficient

I. INTRODUCTION

AIRCRAFT Aircraft propulsion systems often use twin air-intakes to inject atmospheric air into the aero-engines. Such air-intake consists of a Y-shaped twin air-intake duct, which is mounted on either sides of the fuselage of single-engined fighter aircrafts. The two S-shaped limbs of the twin intake duct merged at a section beyond which the duct has a single outlet symmetric about its axis in vertical plane. The air intake of the aircraft supplies the mass flow demand of the engine over a range of aircraft speeds and altitudes with a high pressure recovery and at minimum flow distortion. The total pressure distortion at the engine face is one of the parameters that contribute to the intake losses [1]. The distortion is a significant cause of premature engine surge as well as ‘buzz’, which subsequently resulting in a drastic reduction in the engine thrust. The distortion also leads to flow non-uniformity, which may cause a range of undesirable

effects including asymmetric loading of the compressor blades. Besides, high angle of attack causes local flow separation and cross-flow in the separated region in the Y-duct and develops bulk swirl. This swirl further causes the compressor surge in the aircraft and is therefore considered as a critical parameter for compressor stability [2].

A number of experiments are reported so far to understand the performance and flow characteristics within the single-limb S-duct diffusers as well as to demonstrate various flow control techniques that alleviate the flow separation problems in it. Lin et al. [3] experimentally studied different types of vortex generating devices for turbulent flow separation control at low speeds. They used submerged vortex generators (wheeler doublet and wishbone type), spanwise cylinders, large eddy breakup (LEBU) device at small angle of attack, and vortex generator jets (VGJ). Reichert and Wendt [4] used tapered-fin vortex generators to control the development of secondary flows. They tested 20 configurations of both co- and counter-rotating arrays of tapered-fin vortex generators to reduce total pressure distortion and improve total pressure recovery within an S-shaped diffusing duct. The best configuration tested had reduced distortion by 50% while improving the pressure recovery by 0.5%.

Sullerey et al. [5] carried out experiments to study the effect of various fences and vortex generator configurations in reducing the exit flow distortion and improving the total pressure recovery in two-dimensional rectangular S-duct diffusers of different radius ratios at a Reynolds number (Re) = 7.8×10^5 . It was observed that the fence height and orientation of tapered fin vortex generators giving the best performance would vary depending upon the centerline curvature.

But the literatures on flow control in twin-limbs Y-duct diffusers are found in scanty. It is, however, well understood that the complex flow pattern in the Y-shaped curved diffuser is further enhanced by a number of interrelated geometrical & dynamical parameters, which make the flow distorted and non-uniform at the exit plane in addition to the chances of flow separation. A common flow separation control method is to add momentum to the near wall flow by redirection of higher momentum from the free-stream or the outer region of the boundary layer. This task can be accomplished through either embedded stream-wise vortices or span-wise vortices. The present investigation is focused on flow control in a Y-duct diffuser using vortex generators (VG).

The purpose of adding VG is to supply the momentum from higher region to lower region by stream-wise vortices generated from VG located just before the separation point, as

Akshoy R. Paul is with the Applied Mechanics Department, Motilal Nehru National Institute of Technology, Allahabad-211004, INDIA (phone: 91-532-2271219; fax: 91-532-2271200; e-mail: arpaul2k@yahoo.co.in).

Pritanshu Ranjan is with the Applied Mechanics Department, Motilal Nehru National Institute of Technology, Allahabad-211004, INDIA (e-mail: pritanshu.ranjan@gmail.com).

Ravi R. Upadhyay is with the Mechanical Engineering Department, Motilal Nehru National Institute of Technology, Allahabad-211004, INDIA (e-mail: upadhyay.raviranjan@gmail.com).

Anuj Jain is with the Applied Mechanics Department, Motilal Nehru National Institute of Technology, Allahabad-211004, INDIA (phone: 91-532-2271209; fax: 91-532-2271200; e-mail: anujjain@mnnit.ac.in).

described by Abdellatif [6]. This allows the separation point to shift further downstream. Shifting the separation point downstream enables the expanded airflow to persist proportionately longer, the flow velocity at the separation point to become slower, and consequently the static pressure to become higher. The static pressure at the separation point governs over all pressures in the entire flow separation region. It shifts the separation point downstream; therefore, raise the pressure of the flow separation region.

The objective of the present work is to study the flow control in a Y-duct diffuser (which is used as air-intake) using trapezoidal-shaped VG attached on either both the sidewalls or top and bottom walls of the diffuser at the inflexion plane (planes B and E). Commercially available computational fluid dynamics (CFD) code is modified and is used to simulate the effects of VG in flow improvement of Y-duct diffuser and to find the best configuration of VG for which the diffuser offers maximum performance.

II. EXPERIMENTAL METHODOLOGY

Experiments are performed on Y-duct diffuser (turning angle, $\Delta\beta = 20^\circ$) with and without counter-rotating VG in a low-speed open-circuit type internal flow generation facility. The average inlet flow velocity (U_{avi}) for both limbs of the Y-duct diffuser are maintained at 19.67 m/s for all the cases. The experimental results, thus generated are further used to validate the CFD code.

A. Air-Intake Geometry

A schematic diagram of the Y-duct diffuser with 20° turning angle and an (outlet-to-inlet) area ratio of 1.33 is shown in Fig. 1. The diffuser is designed as per Fox and Kline [7] and is based on linear area-ratio from inlet to exit. The inlet area (A_i) of the test diffuser was chosen as $75 \times 75 \text{ mm}^2$. Straight length of 75 mm is added to both the inlets and the outlet for proper boundary layer growth. The cross-sectional area of both the limbs increases till the two limbs merge at plane-C. From the plane C, the duct is tapered to an outlet width of 200 mm at plane D. The area ratio for the Y-duct is 1.33, which is calculated from inlet (plane-A or F) to outlet (plane-D) of the duct. Figures

B. Vortex Generators

Two different sizes of vortex generators (VG1 and VG2) are designed as suggested by Ahmad and Watterson [8] and are furnished in table 1. All notations of VG are shown in Fig. 2. All VG are fabricated from 0.8 mm thick aluminum sheet. The maximum height (h_2) of the VG is chosen as 6.55 mm. The minimum boundary layer thickness developed at the duct inflexion plane is measured as 7 mm. Hence the vortex generators are fully submerged in the boundary layer and inject momentum into the flow by locally producing small vortices.

TABLE I
DESIGN PARAMETERS OF SUBMERGED VORTEX GENERATORS

Type	β ($^\circ$)	h_1 (mm)	h_2 (mm)	L (mm)	ℓ (mm)	λ (mm)
SVG1	13.5	2.0	4.0	11.0	10.7	21
SVG2	27.0	3.0	6.55	18.0	11.8	28

*Width of SVG, $b = 6 \text{ mm}$ for both SVG-1 and 2.

The effects of VG orientations (counter-rotating and co-rotating) are also investigated in the study. The orientations are decided depending upon the directions of vortices shedding into the downstream of flow in the Y-duct diffuser. Arrays of VG arranged in both the orientations are shown in Fig. 3 and Fig. 4. Literature reveals that the wishbone type solid vortex generators described in Paul et al. [9] created their own losses, but the VG presented here being very thin in cross section generate very less losses.

III. COMPUTATIONAL METHODOLOGY

Detailed parametric analysis is carried out for the Y-duct diffuser geometry with and without co-rotating vortex generators using commercial CFD software. The computation with such a curvilinear nature requires careful investigation of the duct and understanding of flow physics to develop an appropriate mesh, which is capable of resolving all important flow characteristics at different length scales.

A. Mesh Generation

Commercial software is used for grid generation of Y-duct geometry with and without vortex generators. To get a major part of the computational domain as a structured mesh, hexahedron meshing is done. Grid independency is checked to ensure the computational solutions are independent of grid sizes and is furnished in table 1. After a series of simulation carried out with different grid sizes, the final grid size of 175000 cells is found economical, for which the change of static pressure coefficient (C_{SP}) is 0.005% only. Boundary layer scheme is adopted to capture near wall effects.

TABLE II
CHECKING OF MESH INDEPENDENCY

Mesh no.	No. of volume cells	Total CPU time	C_{SP} (%)
1	50400	2 hr 25min	36.468
2	80000	3 hr 15 min	38.764
3	125000	4 hr 10 min	39.184
4	175000	4 hr 50 min	39.291
5	250000	5 hr 35 min	39.293

B. Turbulence Model

The proper selection of turbulence models for any flow computation using CFD demands rapt attention. The $k-\epsilon$ turbulence model belongs to the class of two-equation models, in which model transport equations are solved for two turbulence quantities k and ϵ . The $k-\epsilon$ model is arguably the simplest complete turbulence model, and it has broadest range of applicability. It is incorporated in most commercial CFD codes, and has been applied to a diverse range of engineering

problems [10]. As is the case with all turbulence models, both the concepts and details evolved over time; but Jones and Launder [11] are appropriately credited with developing the 'standard' $k-\varepsilon$ model, with Launder and Sharma [12] providing improved values of the model constants. The term μ_t is called turbulent or eddy viscosity and is introduced in Reynolds averaged Navier-Stokes (RANS) modeling to describe the time-averaged effects of the turbulent stress. According to the widely used two-equation $k-\varepsilon$ model, μ_t can be expressed as follows:

$$\mu_t = \rho C_\mu (k^2/\varepsilon)$$

where C_μ is a constant and k and ε are the local turbulent kinetic energy and its dissipation rate respectively. In order to close the model two other equations are required, namely the transport equations for k and ε .

k -equation:

$$\frac{\partial(\rho U_i k)}{\partial x_i} = \frac{\partial}{\partial x_i} \left[\left(\mu + \frac{\mu_t}{\sigma_k} \right) \cdot \frac{\partial k}{\partial x_i} \right] = P_k - \rho \varepsilon \quad (2)$$

ε -equation:

$$\frac{\partial(\rho U_i \varepsilon)}{\partial x_i} = \frac{\partial}{\partial x_i} \left[\left(\mu + \frac{\mu_t}{\sigma_\varepsilon} \right) \cdot \frac{\partial \varepsilon}{\partial x_i} \right] + C_{\varepsilon 1} \frac{\varepsilon}{k} P_k - C_{\varepsilon 2} \frac{\varepsilon^2}{k} \quad (3)$$

In Eqs. 2 and 3, P_k is the production rate of turbulent kinetic energy, which depends on the turbulent or eddy viscosity μ_t and the velocity distribution. Five closure coefficients according to Launder and Sharma [12] are taken as

$$C_\mu = 0.09, C_{\varepsilon 1} = 1.44, C_{\varepsilon 2} = 1.92, \sigma_k = 1.0, \sigma_\varepsilon = 1.32$$

These values may be not suitable for low Reynolds number flows, or in some local domains of high Reynolds number flows where the damping effect of the surfaces is prominent; in these cases, some corrections would be required. Launder [13] and Hanjalić [14] reported poor performance of 'standard' $k-\varepsilon$ model for a particular class of flows. To improve the performance, the renormalized group (RNG) method has been used to obtain the $k-\varepsilon$ equation from the Navier-Stokes equations [15-17]. Concerning this problem, Renormalization Group (RNG) model is gaining popularity for modelling internal flows; the difference between RNG and $k-\varepsilon$ models mainly results in the substitution of the constant $C_{\varepsilon 1}$ in Eq. 3 with the following expression:

$$C_{\varepsilon 1} = C_{\varepsilon 1}^0 - \frac{\eta(1-\eta/\eta_0)}{1+\beta\eta^3} \quad (4)$$

where $C_{\varepsilon 1}^0 \approx 1.44$, $\eta_0 \approx 4.4$, $\beta \approx 0.015$ and

$$\eta = (k/\varepsilon) \sqrt{P_k/\mu} \quad (5)$$

Through Eqs. 4 and 5, the production term in Eq. 3 is modified in such a way that it properly accounts for the larger dissipation rate experienced in the laminar regions near solid surfaces. Detailed information about the application of RNG

model is available in [18], according to which the values of five closure coefficients stemming from RNG analysis are

$$C_\mu = 0.0845, C_{\varepsilon 1} = 1.42, C_{\varepsilon 2} = 1.68, \sigma_k = \sigma_\varepsilon = 0.72$$

In the RNG $k-\varepsilon$ model, there is also an additional term in the ε equation, which is an ad hoc model, not derived from RNG theory. It is the term which is largely responsible for the difference in the performance of the standard and RNG models. Turbulent mixing is largely suppressed by the proximity of a wall boundary and the $k-\varepsilon$ model however does not represent this effect and breaks down below the log layer. The turbulence energy k certainly goes down to zero at the wall but fixing the unknown finite value of the ε at wall is not so obvious.

C. Validation of CFD Code

The flow field of the Y-duct diffuser without SVG is preliminarily predicted using three turbulence models, namely, standard $k-\varepsilon$, renormalized group (RNG) $k-\varepsilon$ and shear stress transport (SST) $k-\omega$ models with the experimentally measured skewed inlet velocity profile as input. Here, k is the turbulent kinetic energy (m^2/s^2), ε is turbulent kinetic energy dissipation rate (m^2/s^3), and ω is the specific dissipation rate (s^{-1}). But the validation results (Fig. 5) shows that the computational results predicted by RNG $k-\varepsilon$ are in better agreement with the experimental results. This may be due to the superior capability of RNG $k-\varepsilon$ model to pick the transverse pressure gradients in the ducts having streamline curvature [19].

D. Solution Scheme

To achieve faster convergence, an implicit solution scheme is used in combination with an algebraic multigrid method. The second-order upwind discretization scheme is employed for all equations, which achieves higher accuracy in results. Velocity-pressure coupling is done by pressure-velocity correlation using a 'semi-implicit method for pressure-linked equations' (SIMPLE) algorithm [20]. Scarborough condition is satisfied using under-relaxation factors for all equations. Continuous monitoring of residuals is done for continuity, x -velocity, y -velocity, z -velocity, k , and ε equations. Convergence criteria are set as 10^{-8} for all solutions.

E. Boundary Conditions

Experimental inlet velocity profile measured for Y-duct diffuser is considered as input for the velocity inlet in the CFD simulation. To evaluate relative performance, zero gauge pressure is set as exit condition for all simulations. To specify the turbulence quantities, like the turbulence kinetic energy (k) and the turbulence dissipation rate (ε), two relations are used:

$$k = 1.5(U_{avi} I)^2 \quad (6)$$

$$\varepsilon = (C_\mu^{3/4} k^{3/2})/L \quad (7)$$

where, L =turbulence length scale= $0.07L_c$, L_c = characteristic length,

I = turbulence intensity = $0.16(\text{Re})^{-1/8}$, C_μ =turbulence model constant.

No-slip boundary condition is defined at the duct walls. Near-wall modeling is done using enhanced wall treatment method to account for the boundary layers formed during grid generation. Enhanced wall treatment, which combines two-layer model with enhanced wall functions to resolve the laminar sub-layer.

IV. RESULTS AND DISCUSSION

Both the experimental and computational results are presented in the following sections in terms of various performance parameters of the Y-duct diffuser. All the values are compared with the corresponding values reported for bare Y-duct diffuser (i.e., duct without VG). The results of bare Y-duct diffuser and Y-duct with counter-rotating SVG are found experimentally, whereas, the same with co-rotating VG are found computationally.

A. Static Pressure Recovery

Static pressure recovery coefficient (CPR) is described as the ratio of rise in average static pressure with respect to the inlet to the average dynamic pressure at inlet. Precisely,

$$C_{PR} = (p_s - p_{si}) / (0.5 \rho U_{avi}^2) \quad (8)$$

where p_s and p_{si} are the static pressure at any point and at inlet respectively, and ρ is the air density. Fig. 6 shows the variation of CPR along the centerline length (C_L) of the Y-duct diffuser with various VG combinations. As compared to the bare duct, the diffusers with all the combinations of VG show improvement in static pressure recovery. Y-duct diffuser with VG-2 attached to both sidewalls in counter-rotating fashion offers maximum increase in C_{PR} (4.54%), while the same VG attached to top and bottom walls in co-rotating sequence offers only 1.97% increase in C_{PR} as compared to bare duct.

B. Total Pressure Loss

Total pressure loss coefficient is defined as the ratio of total pressure loss with respect to the inlet to the average dynamic pressure at inlet. It is expressed as

$$C_{TL} = (p_{ti} - p_t) / (0.5 \rho U_{avi}^2) \quad (9)$$

where p_t and p_{ti} are the total pressure at any point and at inlet respectively.

Fig. 6 (a) depicts C_{TL} variation along the centerline length of the Y-duct diffuser with VG attached to both sidewalls. An interesting fact is observed here. The duct with VG-2 (counter-rotating) for which C_{PR} is reported maximum, unexpectedly offers maximum total pressure loss. An increase in height of the VG simultaneously causes two effects: one is to reduce drag resulting from delayed flow separation and another is to increase drag by the VG itself. These two effects are balanced when the VG's height is optimum. Here, the addition of VG causes total pressure loss for all cases except for VG-2 (co-rotating) combination, where a 3.2% reduction in C_{TL} is reported. However the same is not the case when VG attached to top and bottom walls of the duct as shown in Fig. 6 (b). Unlike both sidewalls where a strong pressure gradient is developed, the VG attached to the top and bottom walls

primarily helps in orienting the flowfield, thereby making it uniform at the downstream. Hence the variation C_{TL} in Fig. 6 (b) is marginal.

C. Distortion Pressure Coefficient

The total pressure distortion causes surge or buzz at the exit of the Y-duct (or known as 'aerodynamic inlet plane'-AIP) and is responsible for the intake losses. This phenomena leads to a range of undesirable effects including asymmetric loading of the compressor blades. The distortion is designated in terms of distortion coefficient (DC_{60}) in the worst 60° sector and is calculated at the intake exit cross-section (or AIP) as follows:

$$DC_{60} = (p_{te} - p_{60}) / (0.5 \rho U_{avi}^2) \quad (10)$$

where p_{te} are the total pressure at the duct exit and p_{60} represents the total pressure at the worst 60° sector at the duct exit.

TABLE III
EFFECTS OF VG ON PERFORMANCE PARAMETERS

VG sequence	Location	DC_{60}	S_{io}	σ	θ mm
No VG	--	0.259	0.010	5.420	2.60
VG-1 (counter)	Sidewalls	0.253	0.011	5.359	2.34
	Top-bottom	0.248	0.011	5.270	2.56
VG-1 (co-rot.)	Sidewalls	0.249	0.011	5.374	2.21
	Top-bottom	0.223	0.011	5.208	2.48
VG-2 (counter)	Sidewalls	0.232	0.011	4.972	1.69
	Top-bottom	0.237	0.017	3.593	2.47
VG-2 (co-rot.)	Sidewalls	0.228	0.013	5.370	1.17
	Top-bottom	0.217	0.017	3.438	2.50

The use of VG on the inner surface of the individual S-limbs promotes better mixing of two flow fields, and results a decrease in DC_{60} values in Y-duct diffuser. Proper orientation of VG and its correct height are necessary to obtain the maximum reduction in DC_{60} . It is seen from table 3 that the DC_{60} values reduce for all VG combinations as compared to the bare duct. But maximum reduction in DC_{60} (12% and 16%) is reported while VG-2 (co-rotating) are attached at sidewalls and top-bottom walls of the Y-duct diffuser respectively.

D. Secondary Flow Non-uniformity

The non-uniformity index (S_{io}) at AIP can be defined as the average of the sum of secondary velocities (U_{yz} in $y-z$ plane) non-dimensionalized by dividing by the average velocity at the duct inlet.

$$S_{io} = \sum U_{yz} / (n \times U_{avi}) \quad (11)$$

where n is the number of computed data points.

The S_{io} values furnished in table III for various VG combinations do not show any significant change as compared to the bare duct and records only a slight increase with the use of VG. However, for VG-2 combinations attached in co-rotating sequence offers a higher non-uniformity in secondary flow.

E. Axial Flow Non-uniformity

Due to centerline curvature, area diffusion and merging of two S-limbs, the bulk (axial) flow at the downstream of the Y-shaped air intake is not uniform. To calculate the axial flow non-uniformity at a plane, determination of uncertainty in axial velocity (σ) is important. By definition, it is the mean standard deviation in the axial velocity measured at a cross-plane of air-intake and is expressed as

$$\sigma = \sqrt{\sum (U_x - U_{xav})^2 / n} \quad (12)$$

where U_x is the longitudinal velocity, U_{xav} is the average of longitudinal velocity, and n is the number of measured or computed values at duct exit plane.

It is observed from table 3 that the non-uniformity of secondary flow in y - z plane of Y-duct diffuser decreases with all VG combinations. The VG helps in re-distributing the axial flow in the Y-duct diffuser by injecting the co-rotating vortices from its top and bottom walls. As a result, maximum reduction (36.57%) is possible with VG-2 (counter-rotating) when attached to top and bottom walls.

F. Momentum Thickness

Table III, in addition, gives momentum thickness (θ) values, which is an indicative of momentum scarcity in the boundary layer. Scarcity in momentum increases the chances of flow separation in Y-duct diffusers. A careful monitoring of θ helps to evaluate the delay in flow separation. Since a strong pressure gradient exists between both the sidewalls, boundary layer thickness is higher on these walls. Hence the VG attached to the sidewalls are effective in reducing the flow separation. It is seen from table 3 that the use to VG helps in reducing the momentum thickness at the duct outlet (plane D), thereby reduces the chances of flow separation. It is noted that the Y-duct diffuser with best VG configuration (i.e., VG-2 in co-rotating sequence) while attached to both sidewalls records a highest reduction of θ (55%) as compared to the bare duct.

G. Effect of Vortex Generator Height (h_2)

Parametric analysis is carried out to investigate the effects of VG height (h_2) on duct performance. It is found from table 4 that as the h_2 decreases, the surface area and interference of the flow decreases, hence, the corresponding parasitic drag also decreases. This helps in further increasing in C_{SP} and reducing C_{TL} . It also helps in reducing the axial flow non-uniformity (σ) further by a fair margin.

TABLE IV
EFFECTS OF VORTEX GENERATOR HEIGHT ON PERFORMANCE PARAMETERS
WHILE ATTACHED TO BOTH SIDEWALLS

VG height (h_2)	% increase in C_{PR}	% decrease in C_{TL}	%Change in σ
VG (6.55 mm), i.e. VG-2 (co-rot.)	Ref. value	Ref. value	Ref. value
VG (4.55 mm) co-rot.	2.51	0.86	-12.4
VG (2.55 mm) co-rot.	5.81	7.43	-30.9

V. CONCLUSIONS

The following conclusions can be drawn from the present study:

- The use of VG if attached to sidewalls helps in energizing the decelerating boundary layer, thereby reducing flow separation in Y-duct diffuser. But the VG attached to top and bottom walls of the Y-duct diffuser have an effect on flow uniformity at its outlet.
- The orientation of VG plays an equally important role as height (h_2) and angle (β) of VG in enhancing diffuser performance. The increase of VG angle helps in injecting larger vortices into the decelerating boundary layer. The correct orientation ensures better uniformity of the flow, especially at the diffuser outlet.
- The best combination of the Y-duct diffuser is found with VG-2 arranged in co-rotating sequence. If these VG are attached to both sidewalls, an increase in static pressure recovery (3.33%), a drop in total pressure loss (3.20%), a decrease in distortion coefficient (12%) and a reduction in momentum thickness (55%) are achieved. If VG-2 (co-rotating) are attached on top and bottom walls, it ensures maximum reduction (36.58%) in axial flow non-uniformity while maintaining moderate increase in static pressure recovery, maximum reduction in flow distortion (16% and less flow separation in Y-duct diffuser.
- Likewise, the height of VG (h_2) plays an important role in maintaining flow quality at diffuser outlet. As the h_2 is reduced from 6.55 m to 2.55 mm, the parasitic drag is reduced, and hence improves axial flow uniformity by a margin of 30.9% as compared to the bare duct.

ACKNOWLEDGMENT

The authors are thankful to the Department of Science and Technology (DST), Government of India for financial support through DST-FIST grant. The authors are also indebted to the Motilal Nehru National Institute of Technology, Allahabad, India for providing infrastructural and computational supports to carry out the research.

REFERENCES

- [1] J. Seddon, and E. L. Goldsmith, *Intake Aerodynamics*, Collins Professional Books, London, 1985.
- [2] D. D. William, and L. E. Surber, Intake Engine Compatibility, In: Goldsmith, E.L., Seddon (Eds.), *Practical Intake Aerodynamic Design*, Blackwell Scientific Publications, Oxford, pp. 1993, 21-71.
- [3] J. C. Lin, G. V. Selvy, F. G. Howard, "Exploratory study on vortex generator devices for turbulent flow separation control", *AIAA paper No. AIAA-91-0042*, 1991.
- [4] B. A. Reichert, and B. J. Wendt, "Improving diffusing S-duct performance by secondary flow control", *NASA Technical Memorandum 106492*, 1994.
- [5] R. K. Sullerey, S. Mishra, and A. M. Pradeep, "Application of boundary layer fences and vortex generators in improving performance of S-duct diffusers", *ASME J. of Fluids Engineering*, vol. 124, no. 3, pp. 136-142, 2002.
- [6] O. E. Abdellatif, "Experimental study of turbulent flow characteristics inside a rectangular S-shaped diffusing duct", *AIAA paper No. AIAA-2006-1501*, 2006.
- [7] R. W. Fox, and S. J. Kline, "Flow regimes in curved subsonic diffusers", *Journal of Basic Engineering*, vol. 84, pp. 303-316, 1962.
- [8] K. A. Ahmad, J. K. Watterson, J. S. Cole, and I. Briggs, "Sub-boundary layer vortex generator control of a separated diffuser flow", *AIAA paper No. 2005-4650*, 2005.
- [9] A. R. Paul, K. Kuppa, M. S. Yadav, and U. Dutta, "Flow improvement in rectangular air-intake by submerged vortex generators", *Journal of Applied Fluid Mechanics*, vol. 4, no. 2, 2011 (to be published in July 2011).
- [10] S. B. Pope, *Turbulent Flows*, 6th Reprint, Cambridge Univ. Press, NY, 2009, pp. 373-384.
- [11] W. P. Jones, and B. E. Launder, "The prediction of laminarization with a two-equation model of turbulence", *Int. J. of Heat and Mass Transfer*, vol. 15, pp. 301-314, 1972.
- [12] B. E. Launder, and B. I. Sharma, "Application of the energy-dissipation model of turbulence to the calculation of flow near a spinning disc", *Letters of Heat and Mass Transfer*, vol. 1, pp. 131-138, 1974.
- [13] B. E. Launder, Phenomenological Modeling: Present... and Future?, In: J.L. Lumley (Ed.), *Whither Turbulence? Turbulence at the Crossroads*, Springer-Verlag, Berlin, 1990, pp. 439-485.
- [14] K. Hanjalić, "Advanced turbulence closure models: A view of current status and future prospects", *J. of Heat and Fluid Flow*, vol. 15, pp. 178-203, 1994.
- [15] V. Yakhot, and S. A. Orszag, "Renormalized group analysis of turbulence: I. Basic theory", *J. of Scientific Computation*, vol. 1, 1986, pp. 3-51.
- [16] L. M. Smith, and W. C. Reynolds, "On the Yakhot-Orszag renormalization group method for deriving turbulence statistics and models", *Physics of Fluids*, vol. A4, pp. 364-390, 1992.
- [17] L. M. Smith, and S. L. Woodruff, "Renormalization-group analysis of turbulence", *Annual Review of Fluid Mechanics*, vol. 30, pp. 275-310, 1998.
- [18] S. A. Orszag, I. Staroselsky, W. S. Flannery and Y. Zhang, Introduction to renormalization group modeling of turbulence, In: T. B. Gatski, M. Y. Hussaini and J. L. Lumly (Eds.), *Simulation and Modeling of Turbulent Flows*, Oxford Univ. Press, NY, Chapter 4, 1996, pp. 155-183.
- [19] D. Choudhury, Introduction to the renormalization group method and turbulence modeling, *Fluent Technical Memorandum 107*, 1993, Lebanon, NH.
- [20] S. V. Patankar, *Numerical Heat Transfer and Fluid Flow*, Taylor and Francis Publication, London, 1980.

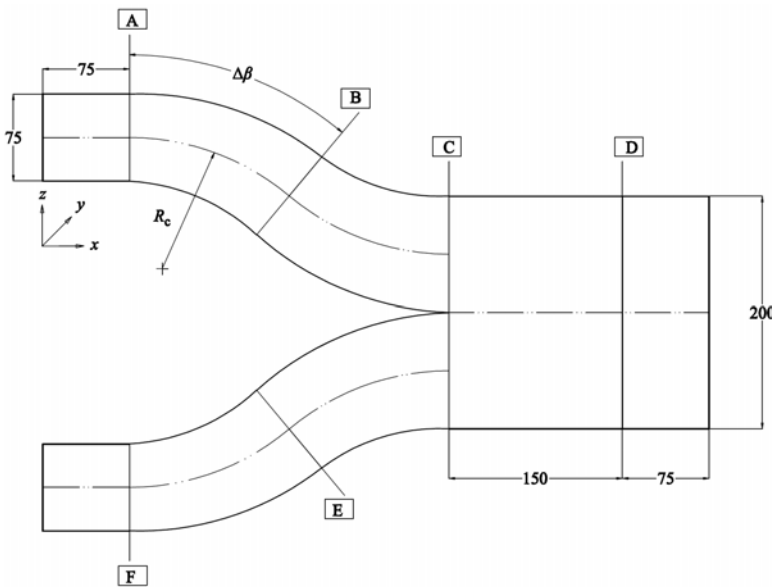


Fig.1 Schematic diagram of a Y-duct diffuser
(Dimensions shown are in mm)

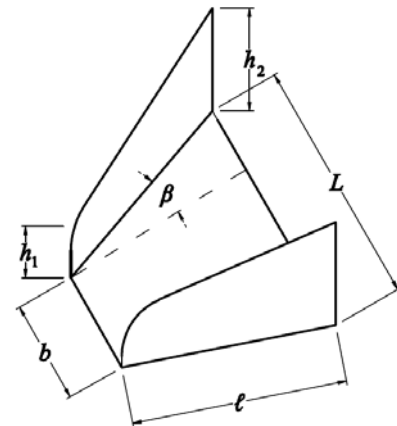


Fig. 2 Schematic diagram of a counter-rotating
vortex generator (VG)

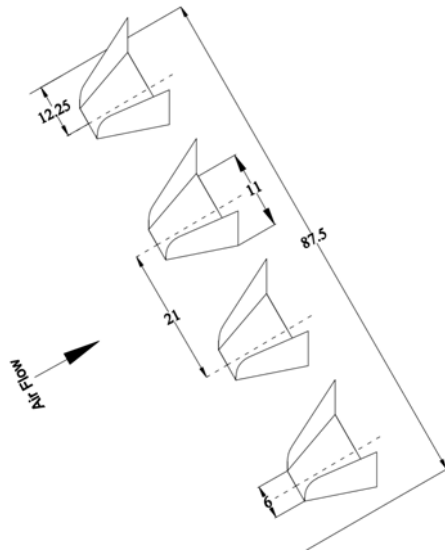


Fig. 3 Experimental arrangement of VG-1 in counter-rotating sequence (all dimensions are in mm)

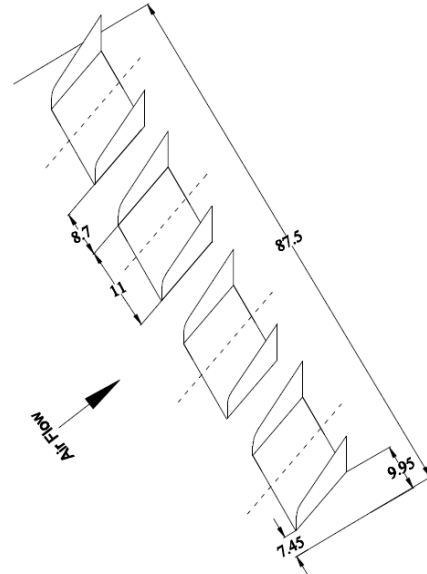


Fig. 4 Computational arrangement of VG-1 in co-rotating sequence (all dimensions are in mm)

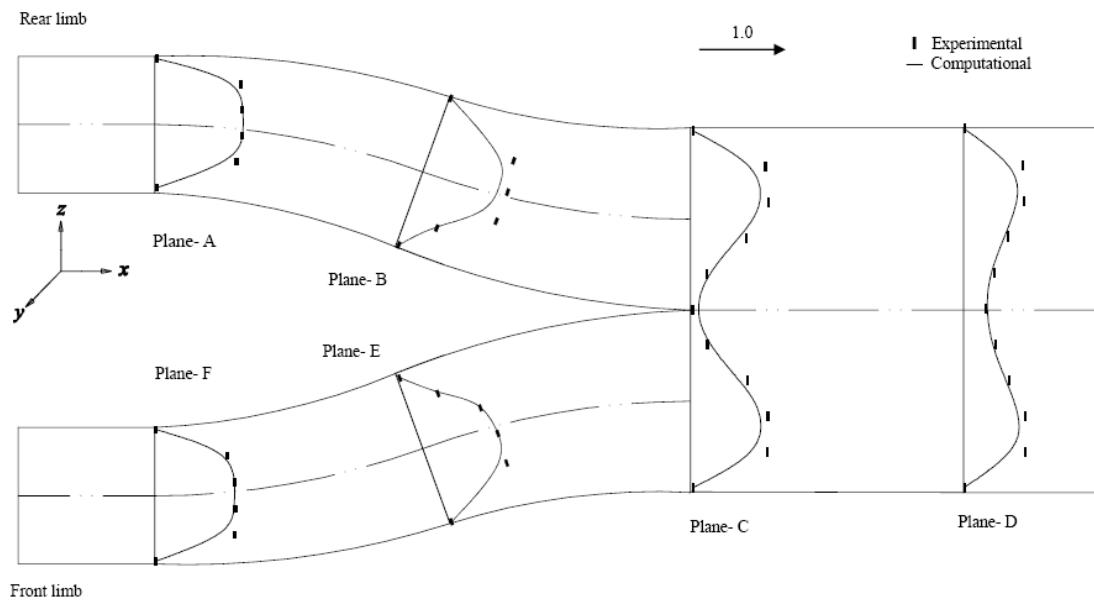


Fig. 5 Normalized mean flow velocity distribution at longitudinal mid-plane

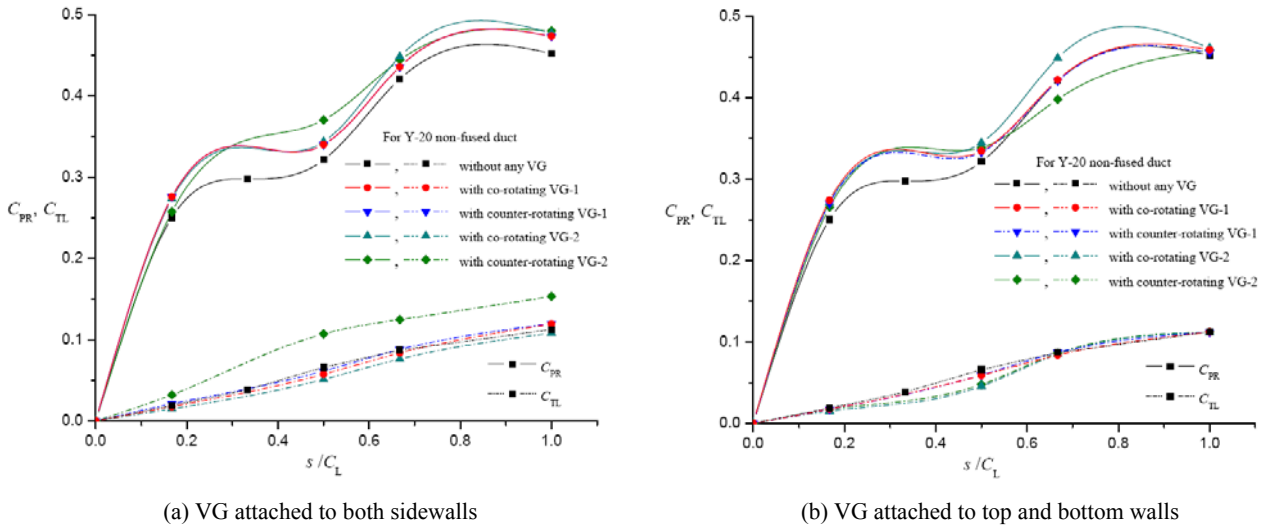


Fig. 6 C_{SP} and C_{TL} distribution for various combinations of VG